Author Manuscript

Author Manuscript

Author Manuscript

Author Manuscript

HHS Public Access

Author manuscript

IEEE Trans Med Imaging. Author manuscript; available in PMC 2017 April 01.

Published in final edited form as:

IEEE Trans Med Imaging. 2016 April ; 35(4): 947–956. doi:10.1109/TMI.2015.2502982.

Theoretical analysis of penalized maximum-likelihood Patlak parametric image reconstruction in dynamic PET for lesion detection

Li Yang [Student Member, IEEE], **Guobao Wang [Senior Member, IEEE]**, and **Jinyi Qi [Fellow, IEEE]**

Department of Biomedical Engineering, University of California, Davis, CA, 95616, USA

Jinyi Qi: qi@ucdavis.edu

Abstract

Detecting cancerous lesions is a major clinical application of emission tomography. In a previous work, we studied penalized maximum-likelihood (PML) image reconstruction for lesion detection in static PET. Here we extend our theoretical analysis of static PET reconstruction to dynamic PET. We study both the conventional indirect reconstruction and direct reconstruction for Patlak parametric image estimation. In indirect reconstruction, Patlak parametric images are generated by first reconstructing a sequence of dynamic PET images, and then performing Patlak analysis on the time activity curves (TACs) pixel-by-pixel. In direct reconstruction, Patlak parametric images are estimated directly from raw sinogram data by incorporating the Patlak model into the image reconstruction procedure. PML reconstruction is used in both the indirect and direct reconstruction methods. We use a channelized Hotelling observer (CHO) to assess lesion detectability in Patlak parametric images. Simplified expressions for evaluating the lesion detectability have been derived and applied to the selection of the regularization parameter value to maximize detection performance. The proposed method is validated using computer-based Monte Carlo simulations. Good agreements between the theoretical predictions and the Monte Carlo results are observed. Both theoretical predictions and Monte Carlo simulation results show the benefit of the indirect and direct methods under optimized regularization parameters in dynamic PET reconstruction for lesion detection, when compared with the conventional static PET reconstruction.

Index Terms

PML reconstruction; lesion detection; Patlak model; dynamic PET

I. Introduction

Statistical reconstruction methods based on the penalized maximum-likelihood (PML) principle have been developed to improve image quality [1]–[3]. A number of metrics have been used to evaluate the quality of the reconstructed PET images, including spatial resolution, noise variance, contrast-to-noise ratio, etc. However, task-specific optimization of the reconstruction parameters are needed in order to achieve the optimal performance. Here we focus on the evaluation of image quality for lesion detection.

Author Manuscript Author Manuscript Author Manuscript Author Manuscript

Based on the theoretical analysis of resolution and noise properties of quadratically regularized PML reconstruction [4]–[6], researchers have derived simplified theoretical expressions for fast evaluation of lesion detectability in PML reconstruction for static PET [7]–[9]. The theoretical results were used to guide the design of a quadratic penalty function to maximize the lesion detectability [10]–[12]. However, the potential of PET is under-utilized by static imaging protocols, which only examine the tracer concentration at a single time point. It is reasonable to expect that dynamic PET, which follows the tracer uptake over a period of time, would provide more accurate information for cancer detection than static PET [13]–[15]. One popular method to analyze dynamic PET data is the Palak graphical model [16]. The slope of the Patlak plot has proved to be a useful quantitative index for characterizing kinetic properties of many PET tracers. Parametric images of the Patlak slope have been used to assist lesion detection [17]. The conventional method to generate Patlak parametric images is to reconstruct a sequence of dynamic images first and then perform Patlak analysis pixel-by-pixel, which we refer to as the indirect method. Alternatively, direct reconstruction methods estimate Patlak parametric images directly from dynamic sinogram data by incorporating the Patlak model into the image reconstruction procedure [18].

To explore the full potential of dynamic PET reconstruction, both indirect and direct methods need to be optimized for the specified clinical application. Here we focus on the task of detecting small lesions (10 mm or smaller). Task-based optimization of dynamic PET reconstruction using multiple Monte Carlo reconsturctions is often impractical, due to the high computational cost associated with fully 4D dynamic PET simulation and reconstruction. A better way is to theoretically analyze and predict the properties of different dynamic PET reconstruction methods and use the results to guide the task-based optimization. However, theoretical analysis of reconstruction methods in dynamic PET is more complicated than that in static PET, due to the need of modeling noise propagation from PET activity images to kinetic parametric images. In this work we extend our theoretical analysis of static PET reconstruction to dynamic PET. We derive simplified theoretical expressions to compute the lesion detectability for a signal-known-exactly and background-known-exactly (SKE/BKE) task in Patlak parametric images reconstructed by either direct or indirect methods, and then use the theoretical predictions to guide the selection of the regularization parameters in both reconstruction methods for lesion detection. Part of this work was presented at the 2015 IEEE International Symposium on Biomedical Imaging [19].

The rest of this paper is organized as follows. In Section II, we first review the theory of dynamic PML reconstruction methods and numerical observers. Then we derive the theoretical expressions for lesion detectability. In Section III, we conduct computer-based Monte Carlo simulations to validate the theoretical results. A discussion is included in Section IV. Finally, we draw conclusions in Section V.

II. Theory

A. Dynamic data model

In emission tomography, the measured sinogram data in the nth frame, $\boldsymbol{y}_n \in \mathbb{R}^{M\times 1}$, can be modeled as a collection of independent Poisson random variables with the expectation $\bar{\boldsymbol{y}}_n \in$

Author Manuscript Author Manuscript Author Manuscript Author Manuscript

$\mathbb{R}^{M\times 1}$ related to the unknown tracer distribution in the nth frame, $\boldsymbol{x}_n \in \mathbb{R}^{N\times 1}$, through an affine transformation

$$\overline{\boldsymbol{y}}_n \equiv E[\boldsymbol{y}_n|\boldsymbol{x}_n]=\boldsymbol{P}\boldsymbol{x}_n+\boldsymbol{r}_n, \quad (1)$$

where M is the number of sinogram bins, N is the number of pixels in each image, $\boldsymbol{P} \in \mathbb{R}^{M\times N}$ is the detection probability matrix with the (i, j)th element equal to the probability of detecting an event from the jth voxel in the ith line of response, and $\boldsymbol{r}_n \in \mathbb{R}^{M\times 1}$ is the expectation of background events (scattered and random events) in the nth frame.

For a set of dynamic data containing T frames, the relationship between the mean dynamic sinogram $\overline{\boldsymbol{y}}=[\overline{\boldsymbol{y}}_1', \overline{\boldsymbol{y}}_2', \ldots, \overline{\boldsymbol{y}}_T']'$ and the dynamic image $\boldsymbol{x}=[\boldsymbol{x}_1', \boldsymbol{x}_2', \ldots, \boldsymbol{x}_T']'$ can be written as

$$\overline{\boldsymbol{y}}=(\boldsymbol{I}_T \otimes P)\boldsymbol{x}+\boldsymbol{r}, \quad (2)$$

where $\otimes$ denotes the Kronecker product, $\boldsymbol{I}_T \in \mathbb{R}^{T\times T}$ is an identity matrix, and $\boldsymbol{r}=[\boldsymbol{r}_1', \boldsymbol{r}_2', \ldots, \boldsymbol{r}_T']'$ are the expected background events. The superscript '′' denotes matrix or vector transpose.

The log Poisson likelihood function of the measured data $\boldsymbol{y}$ is given by

$$L(\boldsymbol{y}|\boldsymbol{x})=\sum_{n=1}^{T} L(\boldsymbol{y}_n|\boldsymbol{x}_n)=\sum_{n=1}^{T}\sum_{i=1}^{M}(\boldsymbol{y}_n)_i \log(\overline{\boldsymbol{y}}_n)_i-(\overline{\boldsymbol{y}}_n)_i, \quad (3)$$

where a constant term that is independent of $\boldsymbol{x}$ is omitted.

B. Patlak graphical model

To analyze dynamic PET data, the Patlak graphical method [16] has been widely used for compartment models that contain at least one irreversible compartment. Under this model, the tracer concentration at time t, $\boldsymbol{c}(t) \in \mathbb{R}^{N\times 1}$, can be represented by a weighted sum of the blood input function $C_p(t)$ and its integral after a sufficient length of time $t^\star$,

$$\boldsymbol{c}(t)=\boldsymbol{\kappa}\int_0^t C_p(\tau)d\tau+\boldsymbol{b}C_p(t),\ t>t^\star, \quad (4)$$

where $\boldsymbol{\kappa} \in \mathbb{R}^{N\times 1}$ and $\boldsymbol{b} \in \mathbb{R}^{N\times 1}$ are the parametric images of the Patlak slope and Patlak intercept, respectively. The slope image $\boldsymbol{\kappa}$ reflects the influx rate of the PET tracer and can be used for lesion detection in FDG PET, since tumors often have higher influx rates than normal tissues.

Author Manuscript Author Manuscript Author Manuscript Author Manuscript

The PET image $\boldsymbol{x}_n$ in the nth frame is related to $\boldsymbol{c}(t)$ by

$$\boldsymbol{x}_n=\int_{t_{sn}}^{t_{en}}\boldsymbol{c}(t)e^{-\lambda t}dt=\boldsymbol{\kappa}\overline{S}_p(n)+\boldsymbol{b}\overline{C}_p(n), \quad (5)$$

where t_{sn} and t_{en} are the start time and end time of frame n, respectively, λ is the decay constant of the PET tracer, and

$$\overline{S}_p(n)=\int_{t_{sn}}^{t_{en}}\int_0^{\tau}C_p(\tau_1)d\tau_1 e^{-\lambda\tau}d\tau, \quad (6)$$

$$\overline{C}_p(n)=\int_{t_{sn}}^{t_{en}}C_p(\tau)e^{-\lambda\tau}d\tau. \quad (7)$$

The relationship between the whole dynamic image sequence $\boldsymbol{x}=[\boldsymbol{x}_1^{'},\boldsymbol{x}_2^{'},\ldots,\boldsymbol{x}_T^{'}]^{'}$ and the Patlak parametric images can be written as

$$\boldsymbol{x}=(\boldsymbol{A}\otimes\boldsymbol{I}_N)\begin{bmatrix}\boldsymbol{\kappa}\\ \boldsymbol{b}\end{bmatrix}, \quad (8)$$

where

$$\boldsymbol{A}=\begin{bmatrix}\overline{S}_p(1) & \overline{C}_p(1)\\ \overline{S}_p(2) & \overline{C}_p(2)\\ \vdots & \vdots\\ \overline{S}_p(T) & \overline{C}_p(T)\end{bmatrix}.$$

Substituting (8) into (2), we can get

$$\overline{\boldsymbol{y}}=(\boldsymbol{A}\otimes\boldsymbol{P})\begin{bmatrix}\boldsymbol{\kappa}\\ \boldsymbol{b}\end{bmatrix}+\boldsymbol{r}. \quad (9)$$

Ignoring the constant term, the corresponding log-likelihood function is

$$L(\boldsymbol{y}|\boldsymbol{\kappa},\boldsymbol{b})=\sum_{n=1}^{T}\sum_{i=1}^{M}(\boldsymbol{y}_n)_i\log(\overline{\boldsymbol{y}}_n)_i-(\overline{\boldsymbol{y}}_n)_i, \quad (10)$$

Author Manuscript Author Manuscript Author Manuscript Author Manuscript

Noted that equation (10) is the log-likelihood function of data $\boldsymbol{y}$ with respect to the Patlak parameters $\boldsymbol{\kappa}$ and $\boldsymbol{b}$, while equation (3) is the log-likelihood function of data $\boldsymbol{y}$ with respect to the dynamic image $\boldsymbol{x}$.

C. Indirect reconstruction

Given a set of measured dynamic sinogram data, the conventional indirect method to generate Patlak parametric images is to first reconstruct the dynamic images frame-by-frame and then estimate the Patlak parametric images pixel-by-pixel using least squares (LS). To reconstruct the image for frame n, PML is used to find the solution maximizing the sum of the log-likelihood function and a roughness penalty:

$$\hat{\boldsymbol{x}}_n(\boldsymbol{y}_n) = \arg\max_{\boldsymbol{x}_n \geq 0} [L(\boldsymbol{y}_n|\boldsymbol{x}_n) - \beta_x \phi(\boldsymbol{x}_n)]. \quad (11)$$

β_x is a parameter that controls the degree of the regularization, $\phi(\boldsymbol{x}_n)$ is the penalty function. While the above equation uses a frame-independent β_x for simplicity, the following analysis is directly applicable to reconstructions with β_x varying across different frames. We focus on commonly used quadratic penalty functions because quantitative studies have not found that edge-preserving penalty functions provide improvement to lesion detection tasks [20], [21]. The quadratic penalty function is expressed as

$$\phi(\boldsymbol{x}_n) = \frac{1}{2} \boldsymbol{x}_n' \boldsymbol{R} \boldsymbol{x}_n, \quad (12)$$

where $\boldsymbol{R}$ is a positive semi-definite matrix. Performing least squares estimation of Patlak parameters from the reconstructed dynamic PET images $\hat{\boldsymbol{x}} = [\hat{\boldsymbol{x}}_1', \hat{\boldsymbol{x}}_2', \ldots, \hat{\boldsymbol{x}}_T']'$, we can get the following results:

$$\begin{aligned} \begin{bmatrix} \hat{\boldsymbol{\kappa}} \\ \hat{\boldsymbol{b}} \end{bmatrix} &= \arg\min_{\boldsymbol{\kappa}, \boldsymbol{b} \geq 0} \tfrac{1}{2} \left\| \hat{\boldsymbol{x}} - (\boldsymbol{A} \otimes \boldsymbol{I}_N) \begin{bmatrix} \boldsymbol{\kappa} \\ \boldsymbol{b} \end{bmatrix} \right\|^2 \\ &= [(\boldsymbol{A}'\boldsymbol{A})^{-1} \boldsymbol{A}' \otimes \boldsymbol{I}_N] \hat{\boldsymbol{x}}. \end{aligned} \quad (13)$$

We refer to the above conventional indirect method as ‘indirect1’.

Since the correlations between pixels are ignored in the Patlak analysis, the indirect1 method may result in very noisy reconstruction. To overcome this problem, we impose a spatial regularization in the pixel-wise Patlak analysis. We refer to this method as ‘indirect2’. Using the quadratic penalty to regularize $\boldsymbol{\kappa}$ and $\boldsymbol{b}$ images, the resultant indirect2 method can be written as

Author Manuscript Author Manuscript Author Manuscript Author Manuscript

$$\begin{bmatrix} \hat{\boldsymbol{\kappa}} \\ \hat{\boldsymbol{b}} \end{bmatrix} = \arg \min_{\boldsymbol{\kappa},\boldsymbol{b}\geq 0} [\frac{1}{2}\|\hat{\boldsymbol{x}} - (\boldsymbol{A} \otimes \boldsymbol{I}_N) \begin{bmatrix} \boldsymbol{\kappa} \\ \boldsymbol{b} \end{bmatrix}\|^2 + \beta_\kappa \phi(\boldsymbol{\kappa}) + \beta_b \phi(\boldsymbol{b})], \quad (14)$$

where $\hat{\boldsymbol{x}}$ represents the dynamic PET images obtained using (11) with a spatial regularization parameter β_x, $\beta_{\boldsymbol{\kappa}}$ and β_b are the regularization parameters on $\boldsymbol{\kappa}$ and $\boldsymbol{b}$, respectively. In total, there are three regularization parameters β_x, $\beta_{\boldsymbol{\kappa}}$ and β_b, to adjust in the indirect2 method. The quadratic penalty function on $\boldsymbol{\kappa}$ and $\boldsymbol{b}$ can be written in matrix form:

$$\begin{aligned} \beta_\kappa \phi(\boldsymbol{\kappa}) + \beta_b \phi(\boldsymbol{b}) &= \frac{1}{2} \begin{bmatrix} \boldsymbol{\kappa} \\ \boldsymbol{b} \end{bmatrix}' \begin{bmatrix} \beta_\kappa \boldsymbol{R} & \\ & \beta_b \boldsymbol{R} \end{bmatrix} \begin{bmatrix} \boldsymbol{\kappa} \\ \boldsymbol{b} \end{bmatrix} \\ &= \frac{1}{2} \begin{bmatrix} \boldsymbol{\kappa} \\ \boldsymbol{b} \end{bmatrix}' \boldsymbol{R}_d \begin{bmatrix} \boldsymbol{\kappa} \\ \boldsymbol{b} \end{bmatrix}, \end{aligned} \quad (15)$$

where

$$\boldsymbol{R}_d \equiv \begin{bmatrix} \beta_\kappa \boldsymbol{R} & \\ & \beta_b \boldsymbol{R} \end{bmatrix}. \quad (16)$$

The closed-form solution of indirect2 reconstruction is

$$\begin{aligned} \begin{bmatrix} \hat{\boldsymbol{\kappa}} \\ \hat{\boldsymbol{b}} \end{bmatrix} &= \left((\boldsymbol{A} \otimes \boldsymbol{I}_N)' (\boldsymbol{A} \otimes \boldsymbol{I}_N) + \boldsymbol{R}_d \right)^{-1} (\boldsymbol{A} \otimes \boldsymbol{I}_N)' \hat{\boldsymbol{x}} \\ &= (\boldsymbol{A}' \boldsymbol{A} \otimes \boldsymbol{I}_N + \boldsymbol{R}_d)^{-1} (\boldsymbol{A} \otimes \boldsymbol{I}_N)' \hat{\boldsymbol{x}} \\ &= \boldsymbol{B} \hat{\boldsymbol{x}}, \end{aligned} \quad (17)$$

where

$$\boldsymbol{B} \equiv (\boldsymbol{A}' \boldsymbol{A} \otimes \boldsymbol{I}_N + \boldsymbol{R}_d)^{-1} (\boldsymbol{A} \otimes \boldsymbol{I}_N)'. \quad (18)$$

Obviously, the indirect1 method in (13) is a special case of the indirect2 method in (17) with $\beta_{\boldsymbol{\kappa}} = \beta_b = 0$. Note that equation (17) is mostly used for theoretical analysis of indirect2 reconstruction. In practice an iterative algorithm is used to find the solution to (14).

D. Direct reconstruction

Direct methods reconstruct Patlak parametric images directly from dynamic sinogram data in one step by incorporating the Patlak model into the image reconstruction procedure [18].

Author Manuscript Author Manuscript Author Manuscript Author Manuscript

Combining the likelihood function with a quadratic penalty function to regularize $\boldsymbol{\kappa}$ and $\boldsymbol{b}$ images, the direct PML estimate of the Patlak parametric images can be found by

$$\begin{bmatrix} \hat{\boldsymbol{\kappa}} \\ \hat{\boldsymbol{b}} \end{bmatrix} = \arg\max_{\boldsymbol{\kappa},\boldsymbol{b}\geq 0} [L(\boldsymbol{y}|\boldsymbol{\kappa},\boldsymbol{b}) - \beta_\kappa \phi(\boldsymbol{\kappa}) - \beta_b \phi(\boldsymbol{b})], \quad (19)$$

where β_κ and β_b are the regularization parameters on $\boldsymbol{\kappa}$ and $\boldsymbol{b}$, respectively. There is no closed form solution to (19), so an iterative algorithm must be used to obtain the solution.

E. Lesion detection with numerical observer

For a given reconstructed image, a numerical observer computes a scalar test statistic η and compares it with a threshold to determine whether the image is normal (i.e., lesion absent) or abnormal (i.e., lesion present). By varying the threshold, we can plot the receiver operating characteristic (ROC) curve and compute the area under the curve (AUC) to compare detection performance. One popular numerical observer for lesion detection is the channelized Hotelling observer (CHO) [22]. With properly selected channel functions, CHO has been shown to have good correlation with human performance.

To study lesion detectability in dynamic PET, we apply CHO to the Patlak slope image $\hat{\boldsymbol{\kappa}}$ in order to mimic the scenario wherein a human observer examines parametric images to detect a lesion. The test statistic of the CHO is computed by

$$\eta_{\mathrm{CHO}}(\hat{\boldsymbol{\kappa}}) = \boldsymbol{z}'\boldsymbol{U}'\boldsymbol{K}^{-1}(\boldsymbol{U}\hat{\boldsymbol{\kappa}} + \breve{\boldsymbol{n}}), \quad (20)$$

where $\boldsymbol{z}$ is the expected profile of the reconstructed lesion, i.e., $\boldsymbol{z} = E[\hat{\boldsymbol{\kappa}}|H_1] - E[\hat{\boldsymbol{\kappa}}|H_0]$ (H_0 is the null hypothesis representing lesion absent and H_1 is the alternative hypothesis representing lesion present), $\boldsymbol{U}$ denotes a set of frequency-selective channels, $\breve{\boldsymbol{n}}$ is the internal channel noise that models the uncertainty in the human detection process with mean zero and covariance $\boldsymbol{K}_N$ [23]–[25]. $\boldsymbol{K}$ is the covariance of the channel outputs and can be computed by

$$\boldsymbol{K} = \frac{1}{2}\boldsymbol{U}\left(\sum\nolimits_{\hat{\boldsymbol{\kappa}}|H_1} + \sum\nolimits_{\boldsymbol{\kappa}|H_0}\right)\boldsymbol{U}' + \boldsymbol{K}_N, \quad (21)$$

where $\boldsymbol{\Sigma}_{\hat{\boldsymbol{\kappa}}/H_1}$ and $\boldsymbol{\Sigma}_{\hat{\boldsymbol{\kappa}}/H_0}$ are the covariance matrices of $\hat{\boldsymbol{\kappa}}$ under the hypotheses of H_1 and H_0, respectively. Here we assume $\boldsymbol{\Sigma}_{\hat{\boldsymbol{\kappa}}/H_1} = \boldsymbol{\Sigma}_{\hat{\boldsymbol{\kappa}}/H_0}$, since the presence of a small lesion with size less than 10 mm has little effect on the variance of PET data.

The detection performance can be measured by the signal-to-noise ratio (SNR) given by

Author Manuscript Author Manuscript Author Manuscript Author Manuscript

$$\mathrm{SNR}^2_{\mathrm{CHO}} = \boldsymbol{z}' \boldsymbol{U}' \boldsymbol{K}^{-1} \boldsymbol{U}\, \boldsymbol{z}. \quad (22)$$

F. Lesion detectability in dynamic PET reconstruction

Up to this point, we have covered the basic dynamic PET model, indirect and direct dynamic PET reconstruction methods, and the evaluation of lesion detectability using numerical observers. To compute the lesion detectability (i.e., SNR in equation (22)) for different reconstruction methods, we need expressions for $\boldsymbol{z}$ and $\boldsymbol{\Sigma}_{\hat{\boldsymbol{\kappa}}}$ One approach is to reconstruct multiple realizations of simulated or measured data sets; however, the high computational cost associated with fully 4D dynamic PET reconstruction can be prohibitive. In this work we overcome this difficulty by deriving analytical expressions of CHO SNR for both indirect and direct methods. In the following we will first analyze the noise propagation in dynamic reconstructions and then apply the results to the evaluation of lesion detectability, which are the main results of this paper.

For indirect methods, we first obtain the approximate mean and covariance of reconstructed images in each frame by (11) using theoretical results derived in [9] as

$$\boldsymbol{z}_{\hat{\boldsymbol{x}}_n} = E[\hat{\boldsymbol{x}}|H_1] - E[\hat{\boldsymbol{x}}|H_0] = (\boldsymbol{F}_n + \beta_x \boldsymbol{R})^{-1} \boldsymbol{F}_n \overline{\boldsymbol{f}}_{ln} \quad (23)$$

$$\sum\nolimits_{\hat{\boldsymbol{x}}_n} = (\boldsymbol{F}_n + \beta_x \boldsymbol{R})^{-1} \boldsymbol{F}_n (\boldsymbol{F}_n + \beta_x \boldsymbol{R})^{-1}, \quad (24)$$

where $\boldsymbol{F}_n = \boldsymbol{P}' \mathrm{diag}[\frac{1}{\overline{y}_n}] \boldsymbol{P}$ is the Fisher information matrix for frame n, and $\overline{\boldsymbol{f}}_{ln}$ is the expected lesion profile after subtracting the background in frame n. The mean and covariance of the complete dynamic image $\hat{\boldsymbol{x}}$ can be written as

$$\boldsymbol{z}_{\hat{\boldsymbol{x}}} = \begin{bmatrix} \boldsymbol{z}_{\hat{\boldsymbol{x}}_1} \\ \vdots \\ \boldsymbol{z}_{\hat{\boldsymbol{x}}_T} \end{bmatrix}, \ \sum\nolimits_{\hat{\boldsymbol{x}}} = \begin{bmatrix} \sum_{\hat{\boldsymbol{x}}_1} & & \\ & \ddots & \\ & & \sum_{\hat{\boldsymbol{x}}_T} \end{bmatrix}. \quad (25)$$

Applying the linear Patlak estimation in (17), we can derive the mean and covariance of the Patlak parametric images by the indirect methods as

$$\begin{aligned} \boldsymbol{z}^{Indirect}_{\hat{\boldsymbol{\kappa}},\hat{\boldsymbol{b}}} &= \boldsymbol{B} \boldsymbol{z}_{\hat{\boldsymbol{x}}}, \\ \sum\nolimits^{Indirect}_{\hat{\boldsymbol{\kappa}},\hat{\boldsymbol{b}}} &= \boldsymbol{B} \sum\nolimits_{\hat{\boldsymbol{x}}} \boldsymbol{B}'. \end{aligned} \quad (26)$$

Author Manuscript Author Manuscript Author Manuscript Author Manuscript

For direct reconstruction, considering $\boldsymbol{A} \otimes \boldsymbol{P}$ as a single system matrix, the resulting Fisher information matrix for estimating parametric images from the dynamic sinogram $\boldsymbol{y}$ can be computed by

$$\boldsymbol{F} = (\boldsymbol{A} \otimes \boldsymbol{P})' \operatorname{diag}[\frac{1}{\overline{\boldsymbol{y}}}] (\boldsymbol{A} \otimes \boldsymbol{P}). \quad (27)$$

Following the derivations similar to that in static PET reconstruction, the mean and covariance of Patlak parametric images reconstructed by the direct method can be approximated by

$$\begin{aligned} \boldsymbol{z}_{\hat{\boldsymbol{\kappa}},\hat{\boldsymbol{b}}}^{Direct} &= (\boldsymbol{F} + \boldsymbol{R}_d)^{-1} \boldsymbol{F} \overline{\boldsymbol{f}}_{\kappa b}, \\ \sum\nolimits_{\hat{\boldsymbol{\kappa}},\hat{\boldsymbol{b}}}^{Direct} &= (\boldsymbol{F} + \boldsymbol{R}_d)^{-1} \boldsymbol{F} (\boldsymbol{F} + \boldsymbol{R}_d)^{-1}, \end{aligned} \quad (28)$$

where $\overline{\boldsymbol{f}}_{\boldsymbol{\kappa} b}$ is the expected lesion profile after subtracting the background in the Patlak parametric images.

Substituting (26) and (28) into (22), we can obtain the theoretical expressions of the SNR for the indirect and direct reconstructions, respectively. Direct computation of (26) and (28) is impractical as it requires the inversion of a large matrix. We assume the local impulse function and the covariance are locally stationary i.e., shift-invariant in a local neighborhood [6], and then use the fast Fourier transform to compute the expressions in the frequency domain [5]. A derivation for the fast computation of (26) and (28) is given in Appendix A. The theoretical expressions can be used to predict the detection performance for a signal-known-exactly and background-known-exactly (SKE/BKE) task, i.e., the SNR of CHO, to evaluate various system configurations and reconstruction parameters.

III. Simulation Study

A. Simulation setup

We simulated a 2D PET system, which has a geometry similar to a GE Discovery PET/CT 690 scanner. A digital phantom (Fig. 1(a)) was created based on a patient PET/CT image (see Fig. 1 in [11]). We segmented out the breast tissue and lungs. Two lesions were simulated as round hot spots with diameters of 6 mm and 10 mm, respectively. The dynamic scanning protocol consisted of 49 frames: 30 frames of 10 seconds, 10 frames of 60 seconds, and 9 frames of 5 minutes, for a total of 60 minutes. The time activity curves (TACs) assigned to the breast tissue, lungs and tumors (Fig. 1(c)) in the phantom, as well as the blood input function (Fig. 1(b)), were extracted from a real dynamic PET scan of a breast cancer patient with 10 mCi FDG injection. The patient had a 3-cm high-grade invasive ductal carcinoma. Fitted Patlak curves are shown in Fig. 1(d), where a linear relationship can be observed after 20 minutes post injection. The fitted Patlak parameters are shown in Table I. In this study, the last 7 frames (from 25 min to 60 min post injection) were used for the

Author Manuscript Author Manuscript Author Manuscript Author Manuscript

Patlak parametric image reconstruction. The activity images were forward projected to generate dynamic sinograms with proper modeling of the resolution degradation effects, photon attenuation and radioactivity decay. Independent Poisson noise was then added to generate a noisy realization with around 24M total counts over the 60-minute dynamic scan, mimicking a PET scan with 10 mCi FDG injection. We did not include scatters and randoms in the computer simulation here. The impact of this limitation will be discussed in Section IV.

We focus on detection of the smaller tumor in the right breast. The larger tumor in the left breast was simulated for quantification task, and the results will be presented elsewhere [26]. We used a CHO with three difference-of-Gaussian (DOG) channels [27] to evaluate detection performance on the reconstructed Patlak slope image $\boldsymbol{\kappa}$ for indirect and direct methods. We also compared the performance of dynamic PET with that of the last 5-minute static scan. The CHO with the same DOG channels was applied to the static reconstructions to evaluate lesion detectability. The internal noise was modeled as zero-mean Gaussian noise with covariance

$$\boldsymbol{K}_N = \alpha_1 \boldsymbol{I} + \mathrm{diag}[\alpha_2 \sigma_i^2 + \alpha_3 \max_i \{\sigma_i^2\}] \quad (29)$$

where $\boldsymbol{I}$ is the identity matrix and σ_i^2 is the data variance in the ith channel output. The values of the scaling factors $\{\alpha_1, \alpha_2, \alpha_3\}$ were taken directly from the previous work [11] as $\alpha_1 = 1.58 \times 10^4$, $\alpha_2 = 0$, and $\alpha_3 = 0.144$, which resulted in good correlation with human performance. To use the internal noise model with same parameters, we scaled the reconstructed $\boldsymbol{\kappa}$ images and the static activity images to the same mean intensity value as the one in previous work [11] before applying the CHO.

B. Theoretical analysis of different reconstruction methods

We used the theoretical expressions to study the effect of β_x in (11) for static reconstruction and indirect1 reconstruction, the effect of β_x in (11) and $\{\beta_\kappa, \beta_b\}$ in (17) for indirect2 reconstruction, and the effect of $\{\beta_\kappa, \beta_b\}$ in (19) for the direct reconstruction. To compute the Fisher information matrix in (24) and (27), we used the plug-in approach developed in [9], which approximates $1/\bar{\boldsymbol{y}}$ by $1/(\boldsymbol{y} + 1)$. For the indirect2 method, we plotted the theoretical SNR as a function of β_κ and β_b under one β_x value ($=10^{-1}$) in Fig. 2(a). We can see that the maximum SNR is achieved when the regularization on the Patlak intercept image $\boldsymbol{b}$ is strong ($\beta_b \geq 10^{11}$). In Fig. 2(b) we plotted the theoretical SNR of the direct reconstruction as a function of β_κ and β_b. Similarly, the maximum SNR is also achieved when the regularization on the Patlak intercept image $\boldsymbol{b}$ is strong ($\beta_b \geq 10^4$). For both methods, the strong regularization (large β_b value) on the Patlak intercept image reduces noise not only in the intercept image $\boldsymbol{b}$, but also in the Patlak slope image $\boldsymbol{\kappa}$ because of the strong negative correlation between $\boldsymbol{b}$ and $\boldsymbol{\kappa}$. In addition, since the tumor has a higher intercept value than the background, the oversmoothing results in a negative bias in the $\boldsymbol{b}$ image, which in turn increases the tumor contrast in the $\boldsymbol{\kappa}$ image. Both of these improve the lesion detectability in the Patlak slope image. (Example images can be seen in Fig. 6.) In

Author Manuscript Author Manuscript Author Manuscript Author Manuscript

comparison, such improvement in lesion detectability cannot be achieved by post-smoothing the Patlak slope image obtained from the indirect1 method.

In Fig. 3 we plotted the SNR of the indirect2 as a function of β_x with the optimal $\{\beta_\kappa, \beta_b\}$ (i.e., $\mathrm{SNR}(\beta_x) = \max_{\{\beta_\kappa,\beta_b\}} \mathrm{SNR}(\beta_x, \beta_\kappa, \beta_b)$), SNR of the direct method as a function of β_κ with the optimal β_b (i.e., $\mathrm{SNR}(\beta_\kappa) = \max_{\beta_b} \mathrm{SNR}(\beta_\kappa, \beta_b)$), SNR of the indirect1 as a function of β_x, and compared them with the static reconstruction which is a function of β_x. It is interesting to see that the best performance of indirect2 and direct reconstruction are comparable. This indicates that the regularization on the parametric images is important to improve lesion detection for Patlak parametric reconstruction. Both the indirect2 and direct reconstruction, with their own optimal regularization parameters, can greatly improve the SNR compared to the static and indirect1 methods. Note that the indirect2 method has three regularization parameters to adjust, while the direct method has two regularization parameters.

C. Theoretical analysis under different tumor contrasts

To investigate how the performance changes with the tumor-to-background contrast ratio, we scaled the tumor TAC by a factor of 0.2, 0.3, and 0.4 as shown in Fig. 4(a). These modified TACs correspond to tumors with a lower FDG transport rate from blood into tumor cells. The scaling of the tumor TAC is similar to the inverse scaling of the background TAC used by others [28]. We plotted the theoretical SNRs of static, indirect1, indirect2 and direct methods under different tumor-to-background contrast in Fig. 4(b, c, d). The results show that the performance of all reconstructions drops as the tumor-to-background contrast decreases. The rankings among the static, indirect2 and direct reconstructions remain unchanged across different tumor contrast. However, the relative performance of the indirect1 method improves with reduced tumor contrast. When the tumor contrast is low and $\beta_x > 0.1$, the optimal β_κ and β_b values in indirect2 method are very small. In this case the performance of indirect1 method approaches that of the indirect2 method, because the indirect1 method is simply a special case of the indirect2 method with $\beta_\kappa = \beta_b = 0$. The results show that the optimal regularization parameters in each reconstruction method change for different tumor contrast ratios. The optimal regularization parameters also depend on the tumor location and background activity. One solution is to use the theoretical expressions to design a shift variant penalty function similar to what we did for static PET [11]. The design of the optimal shift variant penalty function for indirect and direct reconstruction is beyond the scope of this paper.

D. Validation by Monte Carlo simulation

To verify the theoretical predictions, we reconstructed 200 noisy datasets using the direct method and indirect method with different regularization parameters. The MAP-EM algorithm [29] was used for frame-by-frame reconstructions. A linear least squares estimation was used to generate Patlak parametric images for the indirect1 method. For the indirect2 method, we used an optimization transfer algorithm [30] to find the solution of (14). A nested MAP-EM [31] algorithm was used for the direct reconstruction. Three hundred iterations were used for the MAP-EM algorithm, and 200 iterations with 20 inner-iterations were used for the nested MAP-EM algorithm to ensure all algorithms reached

Author Manuscript Author Manuscript Author Manuscript Author Manuscript

effective convergence. Note that the specific reconstruction algorithms used for different methods are not critical, as long as they are iterated to convergence, because all the objective functions are concave and do not have local optima. All images were reconstructed using a 256×256 image array with 2×2 mm^2 pixels starting from a uniform initial image with intensity equal to 1. We computed the mean and covariance of the channel outputs from 200 pair reconstructed images (i.e., 200 images under H_0 and 200 images under H_1) for different methods, and then calculated the Monte Carlo SNR using equation (22). Figure 5 show the resultant Monte Carlo SNR with standard deviation estimated using a bootstrap method. In general, the Monte Carlo results match the theoretical predictions very well. Figure. 6 shows a set of sample images reconstructed by different methods using weak, moderate, and strong regularization (corresponding to the three Monte Carlo SNR values for each method, as shown in Fig. 5). Clearly both the indirect2 reconstruction (Fig. 6(c)) and direct reconstruction (Fig. 6(d)) using the optimal set of regularization parameters (middle column) achieve the highest SNR for lesion detection. We note that a large β_b in the indirect2 and direct methods can cause some bias in the reconstructed Patlak slope image, especially for the background breast and lung regions. However, such bias does not have a negative impact on the detection performance. In this example, the lesion detectability is actually improved because of the reduction in background noise. The streaky artifacts appeared in the reconstructions under strong regularization is due to the count-dependent resolution properties of PML reconstruction. A spatially-variant, anisotropic penalty can be designed to ensure uniform resolution as in [32] or to further improve detection performance as in [11].

In addition, we applied the theoretical analysis to dual time-point data [33]–[35]. We select two frames (25–30 min and 55–60 min) to perform the indirect and direct reconstruction, and compare the results with those using seven frames (25–60 min) and static reconstruction (the last frame). The theoretical predictions (dashed lines) and Monte Carlo results are also shown in Fig. 5. We can see that even with 2 frames, both indirect2 and direct reconstruction can still improve detection performance by 15% over the conventional static PET reconstruction. However, the performance of the dual time-point data are worse than that of the full dynamic data. A 22% decrease in the performance was observed for the indirect1 method, while a 43% decrease was observed for the indirect2 and direct methods.

IV. Discussion

Our results show that the theoretical expressions provide an accurate prediction of the CHO SNR under different conditions. On one hand, the theoretical analysis confirmed that the direct method can obtain higher lesion detectability than the indirect1 method, which is consistent with previous results in the literature [18], [36]. On the other hand, we found that the indirect2 and direct methods can achieve comparable performance when using their respective optimum regularization parameters. This indicates that for Patlak parametric image reconstruction, it is important to regularize the parametric image. However, to achieve the best performance, the indirect2 method requires tuning of three regularization parameters simultaneously, while the direct reconstruction has only two regularization parameters to adjust. We note that the optimum regularization parameters also depend on the scanner parameters, patient background and lesion characteristics, such as size and shape. Once the information is available, the theoretical formulae allow us to select the patient-specific

Author Manuscript Author Manuscript Author Manuscript Author Manuscript

regularization parameters. While our simulation was performed for a 2D PET scanner without modeling random and scatter events, the theoretical analysis method is directly applicable to fully 3D PET with a proper system matrix accounting spatially-varying sensitivity in 3D PET and a 3D numerical observer model. We do not expect that the inclusion of background events would affect the accuracy of the theoretical predication because the theoretical expressions depend only on the Fisher information matrix. To estimate the Fisher information matrix, we need to know the variance of the prompt data, but not a separate estimate of the background events. Because scatters and random events increase the number of counts of the prompt data, they can improve the accuracy of the variance estimation by the data plug-in method [6]. We have validated the theoretical analysis and penalty design in static PML reconstruction method for fully 3D PET using real patient data with random and scatter events in [12]. In the future we will extend the validation for fully 4D (3D space + 1D time) dynamic PET.

Another factor that affects the optimum regularization parameters are the internal noise model used in the numerical observer. Without internal noise, the CHO would prefer over-smoothed images because the numerical observer can distinguish tiny differences between two reconstructed images. This is inconsistent with human performance. The internal noise model used in this paper was obtained by fitting the CHO performance to a human observer study [11]. However, the theoretical formulae are amendable to other internal noise models as well as other linear observer models.

Another limitation of the simulation study is that we did not model the effect of patient motion. Motion has become a limiting factor on image quality of modern PET scanners, in particularly in lungs and liver where respiratory motion can be substantial. The problem is further complicated in dynamic PET image reconstruction because the tracer distribution is changing over time. We will address this issue by developing a motion-compensated dynamic PET image reconstruction method in the future.

We used the least squares fitting in the indirect methods, because the variances among different frames are comparable in Patlak analysis. However, the theoretical derivation can be easily extended to indirect methods that use weighted least squares (WLS) estimation. In this case, equation (13) becomes

$$\begin{bmatrix} \hat{\boldsymbol{\kappa}} \\ \hat{\boldsymbol{b}} \end{bmatrix} = \arg\min_{\boldsymbol{\kappa},\boldsymbol{b}\geq 0} \left[\frac{1}{2} \left\| \hat{\boldsymbol{x}} - (\boldsymbol{A} \otimes \boldsymbol{I}_N) \begin{bmatrix} \boldsymbol{\kappa} \\ \boldsymbol{b} \end{bmatrix} \right\|_{\boldsymbol{W}}^2 \right]. \quad (30)$$

where $\boldsymbol{W}$ is a weighting matrix which ideally equals to the inverse of the covariance matrix of $\hat{\boldsymbol{x}}$. The indirect1 method in (13) is simply a special case of the WLS method in (30) with an identity weighting matrix. Because it is impractical to use the exact inverse of the covariance matrix in (30), the weighting matrix is often reduced to a diagonal matrix to account for different variances in each voxel across different frames.

Author Manuscript Author Manuscript Author Manuscript Author Manuscript

To assess the difference in performance between the WLS estimation in (30) and the LS estimation in (13), we computed the image variance for each frame from the 200 Monte Carlo datasets under three different β_x, and used the reciprocals of the pixel variances as the weights in (30) to estimate the Patlak parametric images. Then the CHO SNR was evaluated. The results show that even using the estimated image variance as the weights, the WLS method only improved the SNR by 2.5% compared to the LS method, and both the indirect2 and direct method can improve the SNR by 221.3% compared to the WLS method.

Finally, we note that the Patlak model is not accurate for tracers that do not contain an irreversible compartment. In this case, a nonlinear compartment model can be used. Analysis of nonlinear compartment models in dynamic PET will be included in our future work.

V. Conclusion

We have derived simplified theoretical expressions for fast evaluation of lesion detectability in the Patlak parametric image reconstruction by both indirect and direct methods. The theoretical results can be used to optimize penalty functions in dynamic PET reconstruction for lesion detection. Computer simulations show good agreement between the theoretical predictions and the Monte Carlo results. The results also demonstrate the benefit of both indirect and direct dynamic PET reconstruction for lesion detection when compared with static PET reconstruction. In the future we will evaluate the method using real dynamic PET data.

Acknowledgments

This work was supported by NIBIB under grant R01 EB000194.

The authors would like to thank the anonymous reviewers for their helpful suggestions and also thank Will Hutchcroft for proofreading the manuscript. This work is supported by the National Institute of Biomedical Imaging and Bioengineering under grant number R01EB000194.

References

1. Mumcuoglu E, Leahy R, Cherry S, Zhou Z. Fast gradient-based methods for Bayesian reconstruction of transmission and emission PET images. IEEE Trans Med Imag. 1994; 13:687–701.
2. Fessler JA. Penalized weighted least-squares image reconstruction for positron emission tomography. IEEE Trans Med Imag. 1994; 13:290–300.
3. Fessler JA, Hero AO. Penalized maximum-likelihood image reconstruction using space-alternating generalized EM algorithms. IEEE Trans Image Process. 1995; 4:1417–1429. [PubMed: 18291973]
4. Fessler JA, Rogers WL. Spatial resolution properties of penalized-likelihood image reconstruction: space-invariant tomographs. IEEE Transactions on Image Processing. 1996; 5:1346–1358. [PubMed: 18285223]
5. Qi J, Leahy R. A theoretical study of the contrast recovery and variance of MAP reconstructions from PET data. IEEE Trans Med Imag. 1999; 18:293–305.
6. Qi J, Leahy RM. Resolution and noise properties of MAP reconstruction for fully 3-D PET. IEEE Transactions on Medical Imaging. 2000; 19:493–506. [PubMed: 11021692]
7. Bonetto P, Qi J, Leahy RM. Covariance approximation for fast and accurate computation of channelized Hotelling observer statistics. IEEE Transactions on Nuclear Science. 2000; 47:1567–1572.

Author Manuscript Author Manuscript Author Manuscript Author Manuscript

8. Qi J, Huesman RH. Theoretical study of lesion detectability of MAP reconstruction using computer observers. IEEE Trans Med Imag. 2001; 20:815–822.
9. Qi J. Analysis of lesion detectability in Bayesian emission reconstruction with nonstationary object variability. IEEE Trans Med Imag. 2004; 23:321–329.
10. Qi J, Huesman R. Penalized maximum likelihood image reconstruction for lesion detection. Phys Med Biol. 2006; 51:4017–29. [PubMed: 16885621]
11. Yang L, Zhou J, Ferrero A, Badawi R, Qi J. Regularization design in penalized maximum-likelihood image reconstruction for lesion detection in 3D PET. Phys Med Biol. 2014; 59:403–419. [PubMed: 24351981]
12. Yang L, Ferrero A, Hagge R, Badawi R, Qi J. Evaluation of penalty design in penalized maximum-likelihood image reconstruction for lesion detection. Journal of Medical Imaging. 2014; 1:035501–1–035501–7. [PubMed: 26158072]
13. Nieweg O, Pruim J, Van Ginkel R, Hoekstra H, Paans A, Molenaar W, Koops H, Vaalburg W. Fluorine-18-Fluorodeoxyglucose PET imaging of soft-tissue sarcoma. Journal of Nuclear Medicine. 1996; 37:257–262. [PubMed: 8667056]
14. Gupta N, Gill H, Graeber G, Bishop H, Hurst J, Stephens T. Dynamic positron emission tomography with F-18 fluorodeoxyglucose imaging in differentiation of benign from malignant lung/mediastinal lesions. Chest. 1998; 114:1105–1111. [PubMed: 9792584]
15. Dimitrakopoulou-Strauss A, Strauss L, Schwarzbach M, Burger C, Heichel T, Willeke F, Mechtersheimer G, Lehnert T. Dynamic PET 18F-FDG studies in patients with primary and recurrent soft-tissue sarcomas: impact on diagnosis and correlation with grading. Journal of Nuclear Medicine. 2001; 42:713–721. [PubMed: 11337565]
16. Patlak C, Blasberg R, Fenstermacher J. Graphical evaluation of blood-to-brain transfer constants from multiple-time uptake data. Journal of Cerebral Blood Flow and Metabolism. 1983; 3:1–7. [PubMed: 6822610]
17. Kenny L, Vigushin D, Al-Nahhas A, Osman S, Luthra S, Shousha S, Coombes R, AEO. Quantification of cellular proliferation in tumor and normal tissues of patients with breast cancer by [18f] fluorothymidine-positron emission tomography imaging: evaluation of analytical methods. Cancer Res. 2005; 65:10104–10112. [PubMed: 16267037]
18. Wang G, Fu L, Qi J. Maximuma posteriori reconstruction of the Patlak parametric image from sinograms in dynamic PET. Phys Med Biol. 2008; 53:593–604. [PubMed: 18199904]
19. Yang L, Wang G, Qi J. Theoretical analysis of lesion detectability in PML Patlak parametric image reconstruction using dynamic PET. IEEE International Symposium on Biomedical Imaging. 2015:1188–1191.
20. Qi J. Comparison of Lesion Detection and Quantification in MAP Reconstruction with Gaussian and Non-Gaussian Priors. International Journal of Biomedical Imaging. 2006; 2006:1–10.
21. Nuyts J, Michel C, Brepoels L, Ceuninck LD, Deroose C, Goffin K, Mottaghy FM, Stroobants S, Riet JV, Verscuren R. Performance of MAP reconstruction for hot lesion detection in whole-body PET/CT: an evaluation with human and numerical observers. IEEE Trans Med Imag. 2009; 28:67–73.
22. Yao J, Barrett H. Predicting human performance by a channelized hotelling model. SPIE. 1992:161–168.
23. Abbey CK, Barrett HH. Human- and model-observer performance in ramp-spectrum noise: effect of regularization an object variability. J Opt Soc Am A. 2001; 18:473–488.
24. Oldan J, Kulkarni S, Xing Y, Khurd P, Gindi G. Channelized Hotelling and Human Observer Study of Optimal Smoothing in SPECT MAP Reconstruction. IEEE Trans on Nucl Sci. 2004; 51:733–741.
25. Brankov JG. Evaluation of the channelized Hotelling observerwith an internal-noise model in a train-test paradigm for cardiac SPECT defect detection. Phys Med Biol. 2013; 58:7159–7182. [PubMed: 24051342]
26. Yang, L.; Qi, J. Theoretical analysis of lesion quantification in PML Patlak parametricimage reconstruction for dynamic PET. IEEE Medical Imaging Conference; 2015.
27. Abbey CK, Barrett HH, Wilson DW. Observer signal-to-noise ratios for the ML-EM algorithm. SPIE. 1996; 3340:2–13.

Author Manuscript Author Manuscript Author Manuscript Author Manuscript

28. Li Z, Li Q, Yu X, Conti P, Leahy R. Lesion detection in dynamic FDG-PET using matched subspace detection. IEEE Trans Med Imag. 2009; 28:230–240.
29. De Pierro A. A modified expectation maximization algorithm for penalized likelihood estimation in emission tomography. IEEE Trans Med Imag. 1995; 14:132–137.
30. Lange K, Hunter D, Yang I. Optimization Transfer Using Surrogate Objective Functions. Journal of Computational and Graphical Statistics. 2000; 9:1–20.
31. Wang G, Qi J. Acceleration of the direct reconstruction of linear parametric images using nested algorithms. Phys Med Biol. 2010; 55:1505–1517. [PubMed: 20157226]
32. Stayman J, Fessler J. Regularization for uniformspatial resolution properties in penalized-likelihood image reconstruction. IEEE Trans Med Imag. 2000; 19:601–615.
33. Strauss L, Pan L, Cheng C, Haberkorn U, Dimitrakopoulou-Strauss A. Shortened acquisition protocols for the quantitative assessment of the 2-tissue-compartment model using dynamic PET/CT 18F-FDG studies. Journal of Nuclear Medicine. 2011; 52(3):379–385. [PubMed: 21321263]
34. Karakatsanis N, Lodge M, Tahari A, Zhou Y, Wahl R, Rahmim A. Dynamic whole-body PET parametric imaging: I. Concept, acquisition protocol optimization and clinical application. Phys Med Biol. 2013; 58:7391–7418. [PubMed: 24080962]
35. Zhu W, Li Q, Bai B, Conti P, Leahy R. Patlak Image Estimation From Dual Time-Point. IEEE Trans Med Imag. 2014; 33:913–924.
36. Tsoumpas C, Turkheimer FE, Thielemans K. Study of direct and indirect parametric estimation methods of linear models in dynamic positron emission tomography. Med Phys. 2008; 35(4): 1299–309. [Online]. Available: http://www.ncbi.nlm.nih.gov/pubmed/18491524. [PubMed: 18491524]

Appendix A. Fast computation of theoretical SNR

Here we derive approximate expressions for fast computation of (26) and (28). Using results in [9], (23) and (24) can be computed by:

$$\boldsymbol{z}_{\hat{\boldsymbol{x}}_n}=\boldsymbol{Q}'\operatorname{diag}\left[\frac{\boldsymbol{\lambda}_n\boldsymbol{\xi}_n}{\boldsymbol{\lambda}_n+\beta_x\boldsymbol{\mu}}\right], \quad (31)$$

$$\sum\nolimits_{\hat{\boldsymbol{x}}_n}=\boldsymbol{Q}'\operatorname{diag}\left[\frac{\boldsymbol{\lambda}_n}{(\boldsymbol{\lambda}_n+\beta_x\boldsymbol{\mu})^2}\right]\boldsymbol{Q}, \quad (32)$$

where $\boldsymbol{Q}$ is the two-dimensional (or three-dimensional) Kronecker form of the Fourier transform, $\boldsymbol{\lambda}_n$ and $\boldsymbol{\mu}$ are the Fourier coefficients of the column vectors corresponding to the lesion location of $\boldsymbol{F}_n$ and $\boldsymbol{R}$, respectively, $\boldsymbol{\xi}_n$ is the Fourier transform of $\bar{\boldsymbol{f}}_{ln}$. Substituting (31) and (32) into (25), the mean and covariance of the dynamic image $\hat{\boldsymbol{x}}$ can be represented by:

$$\boldsymbol{z}_{\hat{\boldsymbol{x}}}=\begin{bmatrix}\boldsymbol{Q}' & & \\ & \ddots & \\ & & \boldsymbol{Q}'\end{bmatrix}\begin{bmatrix}\operatorname{diag}\left[\frac{\boldsymbol{\lambda}_1\boldsymbol{\xi}_1}{\boldsymbol{\lambda}_1+\beta_x\boldsymbol{\mu}}\right]\\ \vdots \\ \operatorname{diag}\left[\frac{\boldsymbol{\lambda}_T\boldsymbol{\xi}_T}{\boldsymbol{\lambda}_T+\beta_x\boldsymbol{\mu}}\right]\end{bmatrix}, \quad (33)$$

$$\sum\nolimits_{\hat{\boldsymbol{x}}}=\begin{bmatrix} \boldsymbol{Q}' & & \\ & \ddots & \\ & & \boldsymbol{Q}' \end{bmatrix}\begin{bmatrix} \mathrm{diag}\left[\frac{\boldsymbol{\lambda}_1}{(\boldsymbol{\lambda}_1+\beta_x\boldsymbol{\mu})^2}\right] & & \\ & \ddots & \\ & & \mathrm{diag}\left[\frac{\boldsymbol{\lambda}_T}{(\boldsymbol{\lambda}_T+\beta_x\boldsymbol{\mu})^2}\right] \end{bmatrix}\begin{bmatrix} \boldsymbol{Q} & & \\ & \ddots & \\ & & \boldsymbol{Q} \end{bmatrix}. \tag{34}$$

For the indirect reconstruction, we have

$$\boldsymbol{A}'\boldsymbol{A}=\begin{bmatrix} \sum_{i=1}^{T}\overline{S}_p(i)^2 & \sum_{i=1}^{T}\overline{S}_p(i)\overline{C}_p(i) \\ \sum_{i=1}^{T}\overline{S}_p(i)\overline{C}_p(i) & \sum_{i=1}^{T}\overline{C}_p(i)^2 \end{bmatrix}\triangleq\begin{bmatrix} a_{11} & a_{12} \\ a_{12} & a_{22} \end{bmatrix}. \tag{35}$$

Then the mean of Patlak parametric images can be computed by

$$\begin{aligned} \boldsymbol{z}_{\hat{\boldsymbol{\kappa}},\hat{\boldsymbol{b}}}^{Indirect}&=\left((\boldsymbol{A}'\boldsymbol{A}\otimes\boldsymbol{I}_N)+\begin{bmatrix} \beta_\kappa\boldsymbol{R} & \\ & \beta_b\boldsymbol{R} \end{bmatrix}\right)^{-1}(\boldsymbol{A}\otimes\boldsymbol{I}_N)'\boldsymbol{z}_{\hat{\boldsymbol{x}}} \\ &=\begin{bmatrix} a_{11}\boldsymbol{I}_N+\beta_\kappa\boldsymbol{R} & a_{12}\boldsymbol{I}_N \\ a_{12}\boldsymbol{I}_N & a_{22}\boldsymbol{I}_N+\beta_b\boldsymbol{R} \end{bmatrix}^{-1}(\boldsymbol{A}\otimes\boldsymbol{I}_N)'\boldsymbol{z}_{\hat{\boldsymbol{x}}} \\ =\begin{bmatrix} \boldsymbol{Q}' & \\ & \boldsymbol{Q}' \end{bmatrix}&\begin{bmatrix} a_{11}\boldsymbol{I}_N+\beta_\kappa\mathrm{diag}[\boldsymbol{\mu}] & a_{12}\boldsymbol{I}_N \\ a_{12}\boldsymbol{I}_N & a_{22}\boldsymbol{I}_N+\beta_b\mathrm{diag}[\boldsymbol{\mu}] \end{bmatrix}^{-1}\begin{bmatrix} \boldsymbol{Q} & \\ & \boldsymbol{Q} \end{bmatrix}(\boldsymbol{A}\otimes\boldsymbol{I}_N)'\boldsymbol{z}_{\hat{\boldsymbol{x}}}. \end{aligned} \tag{36}$$

Since

$$\begin{aligned} (\boldsymbol{A}\otimes\boldsymbol{I}_N)'&=\begin{bmatrix} \overline{S}_p(1)\boldsymbol{I}_N & \dots & \overline{S}_p(T)\boldsymbol{I}_N \\ \overline{C}_p(1)\boldsymbol{I}_N & \dots & \overline{C}_p(T)\boldsymbol{I}_N \end{bmatrix}=\begin{bmatrix} \overline{S}_p(1)\boldsymbol{I}_N\boldsymbol{Q}'\boldsymbol{Q} & \dots & \overline{S}_p(T)\boldsymbol{I}_N\boldsymbol{Q}'\boldsymbol{Q} \\ \overline{C}_p(1)\boldsymbol{I}_N\boldsymbol{Q}'\boldsymbol{Q} & \dots & \overline{C}_p(T)\boldsymbol{I}_N\boldsymbol{Q}'\boldsymbol{Q} \end{bmatrix} \\ &=\begin{bmatrix} \boldsymbol{Q}' & \\ & \boldsymbol{Q}' \end{bmatrix}\begin{bmatrix} \overline{S}_p(1)\boldsymbol{I}_N & \dots & \overline{S}_p(T)\boldsymbol{I}_N \\ \overline{C}_p(1)\boldsymbol{I}_N & \dots & \overline{C}_p(T)\boldsymbol{I}_N \end{bmatrix}\begin{bmatrix} \boldsymbol{Q} & & \\ & \ddots & \\ & & \boldsymbol{Q} \end{bmatrix}, \end{aligned} \tag{37}$$

substituting (33) and (37) into (36), we can get

Author Manuscript Author Manuscript Author Manuscript Author Manuscript

$$\boldsymbol{z}_{\hat{\boldsymbol{\kappa}},\hat{\boldsymbol{b}}}^{Indirect}=\begin{bmatrix}\boldsymbol{Q}' & \\ & \boldsymbol{Q}'\end{bmatrix}\begin{bmatrix}a_{11}\boldsymbol{I}_N+\beta_\kappa\mathrm{diag}[\boldsymbol{\mu}] & a_{12}\boldsymbol{I}_N\\ a_{12}\boldsymbol{I}_N & a_{22}\boldsymbol{I}_N+\beta_b\mathrm{diag}[\boldsymbol{\mu}]\end{bmatrix}^{-1}\begin{bmatrix}\overline{S}_p(1)\boldsymbol{I}_N & \dots & \overline{S}_p(T)\boldsymbol{I}_N\\ \overline{C}_p(1)\boldsymbol{I}_N & \dots & \overline{C}_p(T)\boldsymbol{I}_N\end{bmatrix}\begin{bmatrix}\mathrm{diag}\left[\frac{\boldsymbol{\lambda}_1\boldsymbol{\xi}_1}{\boldsymbol{\lambda}_1+\beta_x\boldsymbol{\mu}}\right]\\ \dots\\ \mathrm{diag}\left[\frac{\boldsymbol{\lambda}_T\boldsymbol{\xi}_T}{\boldsymbol{\lambda}_T+\beta_x\boldsymbol{\mu}}\right]\end{bmatrix}$$
$$=\begin{bmatrix}\boldsymbol{Q}' & \\ & \boldsymbol{Q}'\end{bmatrix}\begin{bmatrix}a_{11}\boldsymbol{I}_N+\beta_\kappa\mathrm{diag}[\boldsymbol{\mu}] & a_{12}\boldsymbol{I}_N\\ a_{12}\boldsymbol{I}_N & a_{22}\boldsymbol{I}_N+\beta_b\mathrm{diag}[\boldsymbol{\mu}]\end{bmatrix}^{-1}\begin{bmatrix}\sum_{i=1}^T\overline{S}_p(i)\mathrm{diag}\left[\frac{\boldsymbol{\lambda}_i\boldsymbol{\xi}_i}{\boldsymbol{\lambda}_i+\beta\boldsymbol{\mu}}\right]\\ \sum_{i=1}^T\overline{C}_p(i)\mathrm{diag}\left[\frac{\boldsymbol{\lambda}_i\boldsymbol{\xi}_i}{\boldsymbol{\lambda}_i+\beta\boldsymbol{\mu}}\right]\end{bmatrix}. \tag{38}$$

Similarly, the covariance of Patlak parametric images by indirect reconstruction can be computed by

$$\sum_{\hat{\boldsymbol{\kappa}},\hat{\boldsymbol{b}}}^{Indirect}=\begin{bmatrix}\boldsymbol{Q}' & \\ & \boldsymbol{Q}'\end{bmatrix}\begin{bmatrix}a_{11}\boldsymbol{I}_N+\beta_\kappa\mathrm{diag}[\boldsymbol{\mu}] & a_{12}\boldsymbol{I}_N\\ a_{12}\boldsymbol{I}_N & a_{22}\boldsymbol{I}_N+\beta_b\mathrm{diag}[\boldsymbol{\mu}]\end{bmatrix}^{-1}$$
$$\begin{bmatrix}\sum_{i=1}^T\overline{S}_p(i)^2\mathrm{diag}\left[\frac{\boldsymbol{\lambda}_i}{(\boldsymbol{\lambda}_i+\beta_x\boldsymbol{\mu})^2}\right] & \sum_{i=1}^T\overline{S}_p(i)\overline{C}_p(i)\mathrm{diag}\left[\frac{\boldsymbol{\lambda}_i}{(\boldsymbol{\lambda}_i+\beta_x\boldsymbol{\mu})^2}\right]\\ \sum_{i=1}^T\overline{S}_p(i)\overline{C}_p(i)\mathrm{diag}\left[\frac{\boldsymbol{\lambda}_i}{(\boldsymbol{\lambda}_i+\beta_x\boldsymbol{\mu})^2}\right] & \sum_{i=1}^T\overline{C}_p(i)^2\mathrm{diag}\left[\frac{\boldsymbol{\lambda}_i}{(\boldsymbol{\lambda}_i+\beta_x\boldsymbol{\mu})^2}\right]\end{bmatrix}$$
$$\begin{bmatrix}a_{11}\boldsymbol{I}_N+\beta_\kappa\mathrm{diag}[\boldsymbol{\mu}] & a_{12}\boldsymbol{I}_N\\ a_{12}\boldsymbol{I}_N & a_{22}\boldsymbol{I}_N+\beta_b\mathrm{diag}[\boldsymbol{\mu}]\end{bmatrix}^{-1}\begin{bmatrix}\boldsymbol{Q} & \\ & \boldsymbol{Q}\end{bmatrix}. \tag{39}$$

For direct reconstruction, the Fisher information matrix in (27) can be computed by

$$\boldsymbol{F}=(\boldsymbol{A}\otimes\boldsymbol{P})'\mathrm{diag}[\tfrac{1}{\overline{\boldsymbol{y}}}](\boldsymbol{A}\otimes\boldsymbol{P})$$
$$=\begin{bmatrix}\overline{S}_p(1)\boldsymbol{P}' & \dots & \overline{S}_p(T)\boldsymbol{P}'\\ \overline{C}_p(1)\boldsymbol{P}' & \dots & \overline{C}_p(T)\boldsymbol{P}'\end{bmatrix}\begin{bmatrix}\mathrm{diag}[\frac{1}{\overline{\boldsymbol{y}}_1}] & & \\ & \ddots & \\ & & \mathrm{diag}[\frac{1}{\overline{\boldsymbol{y}}_T}]\end{bmatrix}\begin{bmatrix}\overline{S}_p(1)\boldsymbol{P} & \overline{C}_p(1)\boldsymbol{P}\\ \vdots & \vdots\\ \overline{S}_p(T)\boldsymbol{P} & \overline{C}_p(T)\boldsymbol{P}\end{bmatrix}$$
$$=\begin{bmatrix}\sum_{i=1}^T\overline{S}_p(i)^2\boldsymbol{P}'\mathrm{diag}[\frac{1}{\overline{\boldsymbol{y}}_i}]\boldsymbol{P} & \sum_{i=1}^T\overline{S}_p(i)\overline{C}_p(i)\boldsymbol{P}'\mathrm{diag}[\frac{1}{\overline{\boldsymbol{y}}_i}]\boldsymbol{P}\\ \sum_{i=1}^T\overline{S}_p(i)\overline{C}_p(i)\boldsymbol{P}'\mathrm{diag}[\frac{1}{\overline{\boldsymbol{y}}_i}]\boldsymbol{P} & \sum_{i=1}^T\overline{C}_p(i)^2\boldsymbol{P}'\mathrm{diag}[\frac{1}{\overline{\boldsymbol{y}}_i}]\boldsymbol{P}\end{bmatrix}$$
$$=\begin{bmatrix}\boldsymbol{Q}' & \\ & \boldsymbol{Q}'\end{bmatrix}\begin{bmatrix}\sum_{i=1}^T\overline{S}_p(i)^2\mathrm{diag}[\boldsymbol{\lambda}_i] & \sum_{i=1}^T\overline{S}_p(i)\overline{C}_p(i)\mathrm{diag}[\boldsymbol{\lambda}_i]\\ \sum_{i=1}^T\overline{S}_p(i)\overline{C}_p(i)\mathrm{diag}[\boldsymbol{\lambda}_i] & \sum_{i=1}^T\overline{C}_p(i)^2\mathrm{diag}[\boldsymbol{\lambda}_i]\end{bmatrix}\begin{bmatrix}\boldsymbol{Q} & \\ & \boldsymbol{Q}\end{bmatrix}. \tag{40}$$

To simplify the notation, we define a 2×2 block matrix

$$\begin{bmatrix}\boldsymbol{D_{11}} & \boldsymbol{D_{12}}\\ \boldsymbol{D_{12}} & \boldsymbol{D_{22}}\end{bmatrix}\triangleq\begin{bmatrix}\sum_{i=1}^T\overline{S}_p(i)^2\mathrm{diag}[\boldsymbol{\lambda}_i] & \sum_{i=1}^T\overline{S}_p(i)\overline{C}_p(i)\mathrm{diag}[\boldsymbol{\lambda}_i]\\ \sum_{i=1}^T\overline{S}_p(i)\overline{C}_p(i)\mathrm{diag}[\boldsymbol{\lambda}_i] & \sum_{i=1}^T\overline{C}_p(i)^2\mathrm{diag}[\boldsymbol{\lambda}_i]\end{bmatrix}. \tag{41}$$

Author Manuscript Author Manuscript Author Manuscript Author Manuscript

Author Manuscript Author Manuscript Author Manuscript Author Manuscript

Then the mean of the Patlak parametric images by direct reconstruction can be computed by

$$\boldsymbol{z}_{\hat{\boldsymbol{\kappa}},\hat{\boldsymbol{b}}}^{Direct}=(\boldsymbol{F}+\boldsymbol{R}_d)^{-1}\boldsymbol{F}\overline{\boldsymbol{f}}_{\kappa b}$$
$$=\begin{bmatrix} \boldsymbol{Q}' & \\ & \boldsymbol{Q}' \end{bmatrix}\begin{bmatrix} \boldsymbol{D_{11}}+\beta_\kappa \mathrm{diag}[\boldsymbol{\mu}] & \boldsymbol{D_{12}} \\ \boldsymbol{D_{12}} & \boldsymbol{D_{22}}+\beta_b \mathrm{diag}[\boldsymbol{\mu}] \end{bmatrix}^{-1}\begin{bmatrix} \boldsymbol{D_{11}} & \boldsymbol{D_{12}} \\ \boldsymbol{D_{12}} & \boldsymbol{D_{22}} \end{bmatrix}\begin{bmatrix} \boldsymbol{Q} & \\ & \boldsymbol{Q} \end{bmatrix}\overline{\boldsymbol{f}}_{\kappa b}.$$

(42)

The covariance of the Patlak parametric images by direct reconstruction can be computed by

$$\sum_{\hat{\boldsymbol{\kappa}},\hat{\boldsymbol{b}}}^{Direct}=(\boldsymbol{F}+\boldsymbol{R}_d)^{-1}\boldsymbol{F}(\boldsymbol{F}+\boldsymbol{R}_d)^{-1}$$
$$=\begin{bmatrix} \boldsymbol{Q}' & \\ & \boldsymbol{Q}' \end{bmatrix}\begin{bmatrix} \boldsymbol{D_{11}}+\beta_\kappa \mathrm{diag}[\boldsymbol{\mu}] & \boldsymbol{D_{12}} \\ \boldsymbol{D_{12}} & \boldsymbol{D_{22}}+\beta_b \mathrm{diag}[\boldsymbol{\mu}] \end{bmatrix}^{-1}\begin{bmatrix} \boldsymbol{D_{11}} & \boldsymbol{D_{12}} \\ \boldsymbol{D_{12}} & \boldsymbol{D_{22}} \end{bmatrix}\begin{bmatrix} \boldsymbol{D_{11}}+\beta_\kappa \mathrm{diag}[\boldsymbol{\mu}] & \boldsymbol{D_{12}} \\ \boldsymbol{D_{12}} & \boldsymbol{D_{22}}+\beta_b \mathrm{diag}[\boldsymbol{\mu}] \end{bmatrix}^{-1}\begin{bmatrix} \boldsymbol{Q} & \\ & \boldsymbol{Q} \end{bmatrix}$$

(43)

Note that the matrices in (38), (39), (42) and (43) are all 2×2 block matrices with diagonal blocks and thus their inverse can be easily computed using following formula:

$$\begin{bmatrix} D_A & D_B \\ D_C & D_D \end{bmatrix}^{-1}=\begin{bmatrix} (D_A-D_BD_D^{-1}D_C)^{-1} & -D_A^{-1}D_B(D_D-D_CD_A^{-1}D_B)^{-1} \\ -D_D^{-1}D_C(D_A-D_BD_D^{-1}D_C)^{-1} & (D_D-D_CD_A^{-1}D_B)^{-1} \end{bmatrix}$$

(44)

where D_A, D_B, D_C, D_D are all diagonal matrices.

Author Manuscript Author Manuscript Author Manuscript Author Manuscript

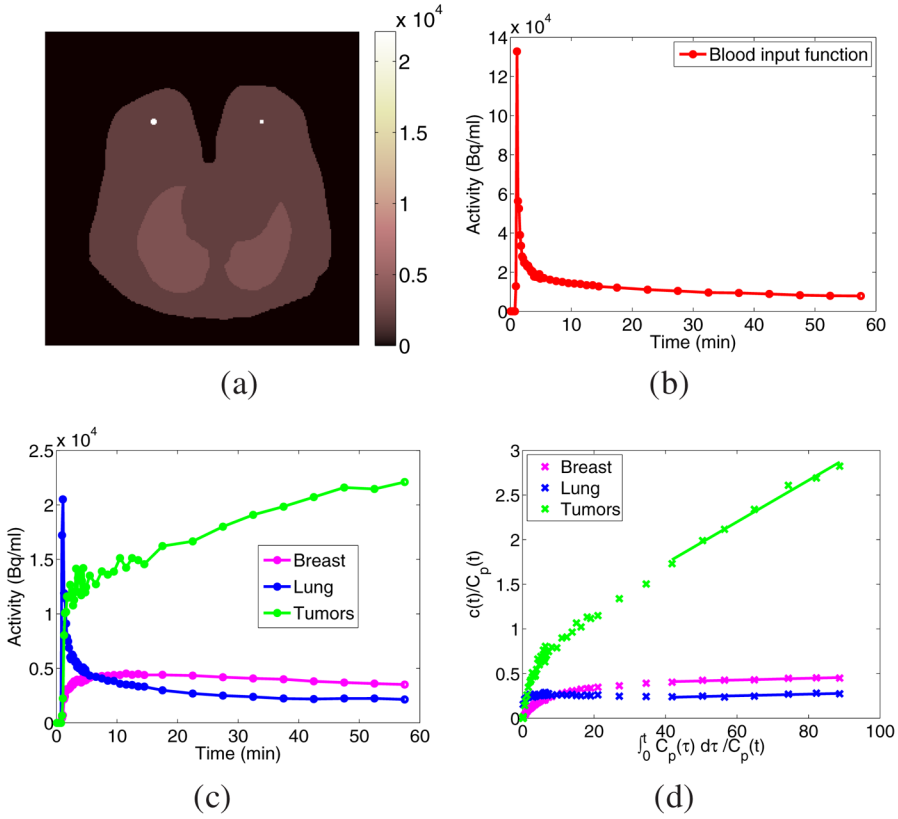

Fig. 1.

(a) Digital phantom (here shows the activity image for the last frame which is from 55 to 60 minutes post injection); (b) the blood input function; (c) TACs for the breast tissue, lungs and tumors; and (d) the fitted Patlak plot.

Author Manuscript Author Manuscript Author Manuscript Author Manuscript

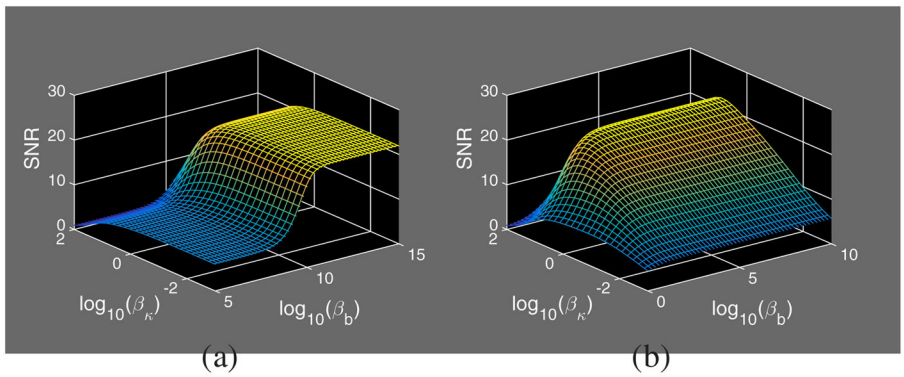

Fig. 2.

Theoretical SNR as a function β_κ and β_b in (a) the indirect2 reconstruction under $\beta_x = 10^{-0.1}$ and (b) direct reconstruction.

Author Manuscript Author Manuscript Author Manuscript Author Manuscript

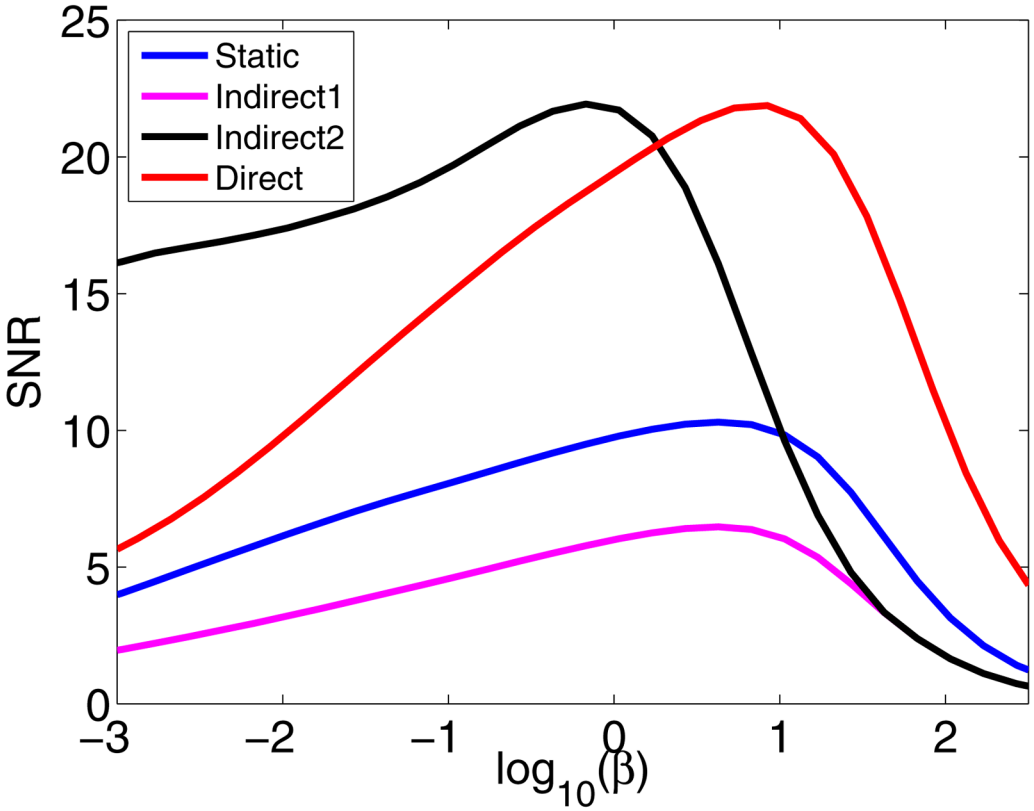

Fig. 3.

Theoretical SNRs of static (as a function of β_x), indirect1 (as a function of β_x), indirect2 (as a function of β_x with the optimal $\{\beta_\kappa, \beta_b\}$) and direct reconstruction (as a function of β_κ with the optimal β_b).

Author Manuscript Author Manuscript Author Manuscript Author Manuscript

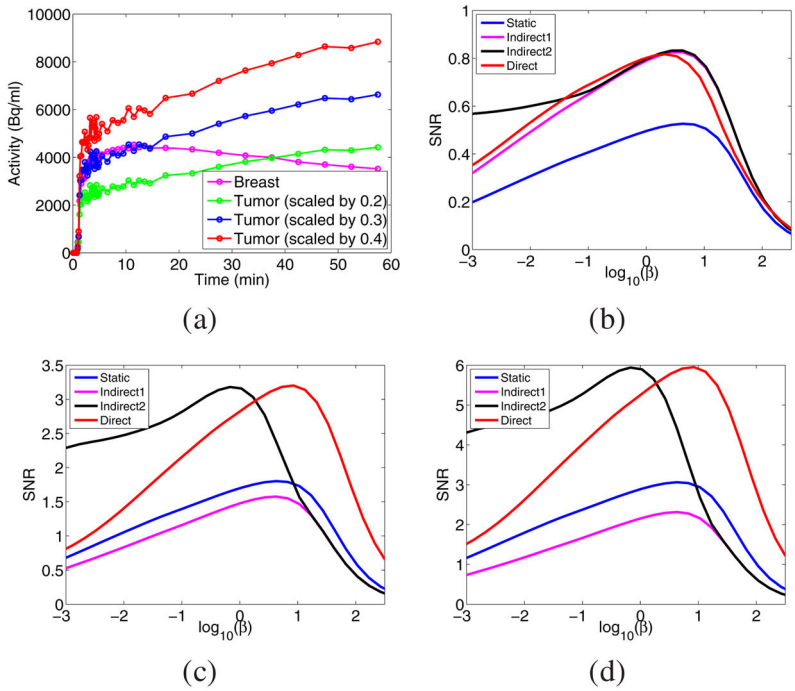

Fig. 4.

(a) Background TAC for the breast tissue and tumor TAC with different scaling factor. (b)–(d) Theoretical SNRs of static (as a function of β_x), indirect1 (as a function of β_x), indirect2 (as a function of β_x with the optimal $\{\beta_x, \beta_b\}$) and direct reconstruction (as a function of β_x with the optimal β_b) for the scaled tumor TAC with a scaling factor of (b) 0.2, (c) 0.3, and (d) 0.4, respectively.

Author Manuscript Author Manuscript Author Manuscript Author Manuscript

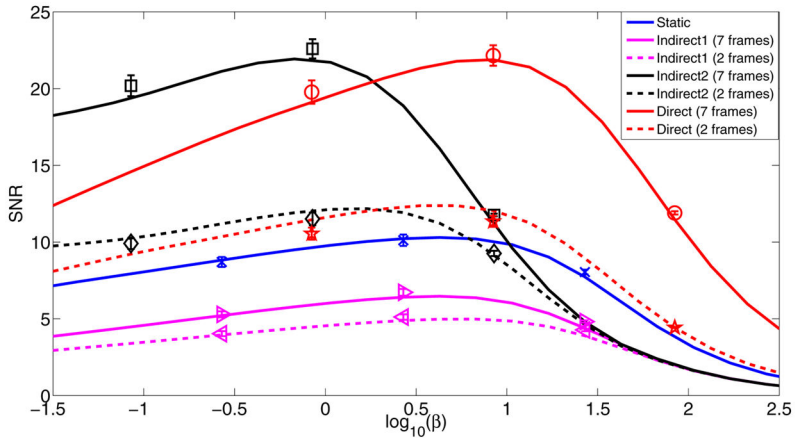

Fig. 5.

Theoretical (solid and dashed curves) and Monte Carlo (‘□’, ‘○’, ‘◇’, ‘★’, ‘×’, ‘▷’, ‘◁’) SNRs of indirect1 (as a function of β_x), indirect2 (as a function of β_x with the optimal $\{\beta_\kappa, \beta_b\}$), direct reconstruction (as a function of β_κ with the optimal β_b) using 7 frames and 2 frames, and static reconstruction (as a function of β_x). The error bars indicate plus and minus one standard deviation estimated by a bootstrap method.

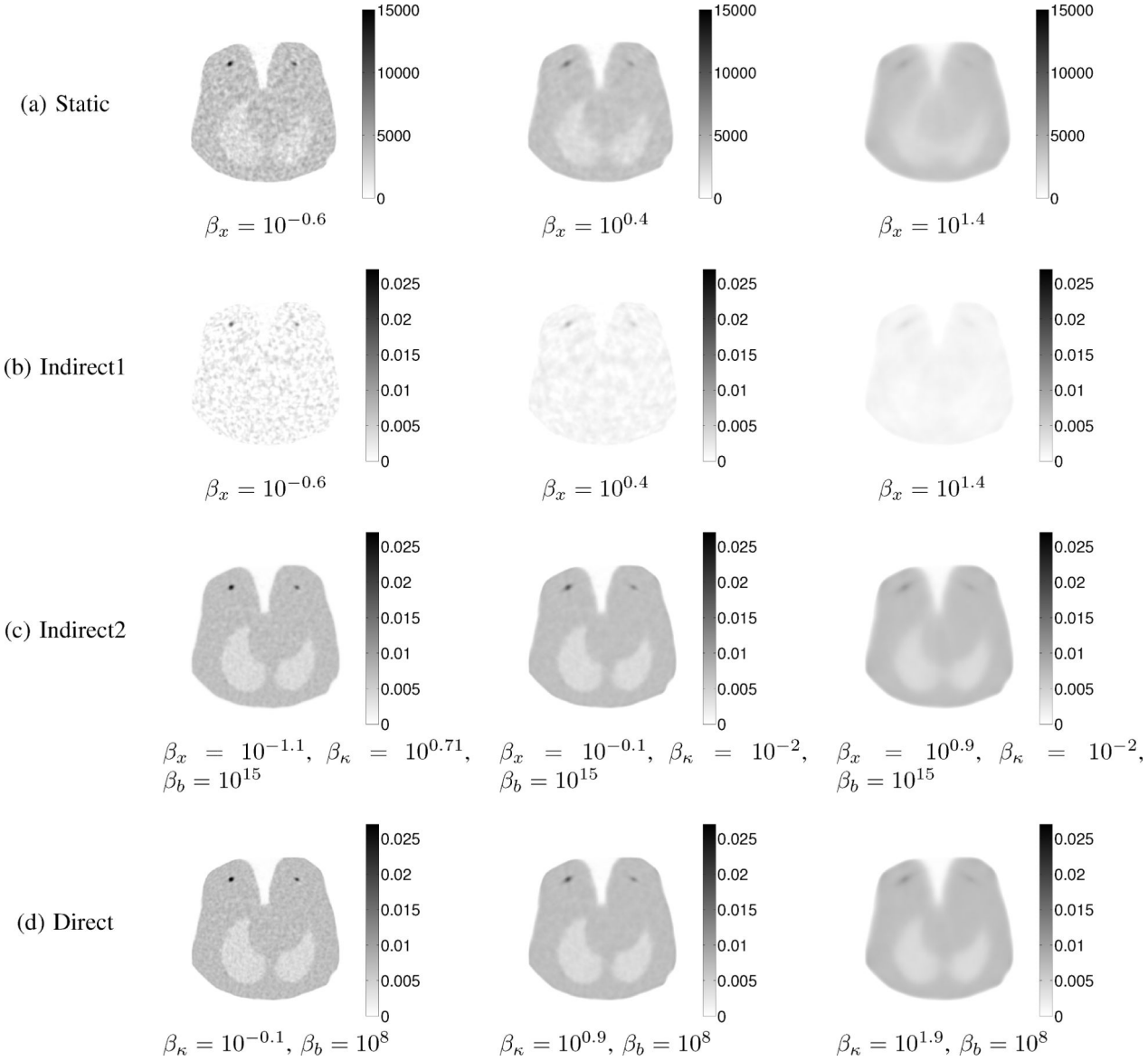

Fig. 6.

Sample reconstruction: static PML reconstructed image of last frame (a), Patlak slope image reconstructed by indirect1 method (b), indirect2 method (c), and direct method (d) under weak (left), moderate (middle), and strong (right) regularization (corresponding to the three Monte Carlo points for each method in Fig. 5).

Author Manuscript Author Manuscript Author Manuscript Author Manuscript

Author Manuscript

Author Manuscript

Author Manuscript

Author Manuscript

TABLE I

Fitted Patlak Parameters for Tacs shown in Fig. 1

	Patlak slope κ	**Patlak intercept b**
Breast	0.001	0.3695
Lung	0.0009	0.1965
Tumor	0.0233	0.8008